RSC Advances

PAPER

View Article Online
View Journal | View Issue

Cite this: *RSC Adv.*, 2020, **10**, 4554

The synthesis of monodispersed M-CeO_2/SiO_2 nanoparticles and formation of UV absorption coatings with them†

Su Xunwen,[a] Zhu Liqun,[a] Li Weiping,[a] Liu Huicong *[a] and Ye Hui[b]

CeO_2/polymer nanoparticles have drawn considerable attention for their excellent UV absorption properties. However, many challenges still exist in the successful incorporation of ceria into the polymer matrix for the easy agglomeration and photocatalytic activity of CeO_2 nanoparticles. Herein, we address these issues by constructing three-layer structured nanoparticles (M-CeO_2@SiO_2) and incorporating them into a polymer matrix through a mini-emulsion polymerization process. During this process, small-sized nano-ceria became uniformly anchored on the surfaces of monodisperse silica particles first, and then the particles were coated with an MPS/SiO_2 shield. The morphology and dispersion of the nanoparticles were investigated using scanning electron microscopy (SEM) and transmission electron microscopy (TEM). The performance of the hybrid films was characterized using UV-vis absorption spectroscopy (UV-vis) and water contact angle (WCA) measurements. Results showed that the M-CeO_2@SiO_2 nanoparticles exhibited a three-layer structure with a mean diameter of 360 nm, and they possess good compatibility with acrylic monomers. After the addition of M-CeO_2@SiO_2, hybrid films exhibited enhanced UV absorption capacity as expected, accompanied by an obvious improvement in hydrophobicity (the water contact angle increased from 84.2° to 98.2°). The results showed that the hybrid films containing M-CeO_2@SiO_2 particles possess better global performance as compared with those containing no particles.

Received 31st October 2019
Accepted 10th January 2020

DOI: 10.1039/c9ra08975f

rsc.li/rsc-advances

1. Introduction

Fluorinated acrylics, which generally contain perfluoroalkyl segments, are typical low surface energy materials with outstanding water/oil repellence characteristics, antifouling properties and satisfactory adhesion on different substrates.[1–5] These unique properties make them ideal candidates for outdoor coatings, which has attracted widespread attention from researchers.[6–8] The purpose of outdoor coatings is to protect the substrates from harsh environments, such as sunlight, rain, and air pollution. Therefore, it is important for fluorine-containing acrylate copolymers to maintain greater protective abilities than simple physical isolation.

Among various harsh environmental factors, ultraviolet rays, which may cause the degradation of organic matrices, leading to the failure of protective coatings, is a major source of damage. Although the polymers themselves are durable in outdoor environments, it is necessary to incorporate some UV absorbers to improve the lifetime and improve the properties of these coatings.[9] Compared with organic UV absorbers that may release environmental pollutants, such as volatile organic compounds (VOC), inorganic nanoparticles such as TiO_2, ZnO and CeO_2 seem to be better choices.[10–14] Among the numerous UV absorbers, ceria nanoparticles are ideal candidates due to their excellent UV absorption ability, visible light transparency and lower light refractive index.[15–18] Several studies have been published on the incorporation of CeO_2 nanoparticles into polymer latex to shield UV light.[19–21] Most of these studies achieved good dispersion of cerium oxide *via* physical blending or modification with ligands or hydrogen bonds, such as citric acid, polyethylene glycol and poly(acrylate acid).[22–25] For hybrid latex obtained using these methods, the interaction between ceria nanoparticles and the organic matrix are weak, making the long-term stability of the system open to question. To the best of our knowledge, although several approaches have been reported for the preparation of CeO_2/polyacrylate hybrid latex, the use of ceria in fluorinated polyacrylate coatings has been seldom reported.

Constructing core–shell structures is commonly used in nano-modification. In this way, the surfaces of nanoparticles are covered with a layer of other materials for protection or modification.[26–30]

[a]*Key Laboratory of Aerospace Materials and Performance (Ministry of Education), School of Materials Science and Engineering, Beihang University, Beijing 100191, China. E-mail: liuhc@buaa.edu.cn; Fax: +861082317113; Tel: +861082317113*

[b]*Aerospace Research Institute of Materials and Processing Technology, No. 1 South Dahongmen Road, Beijing, 100076, China. E-mail: yehui@buaa.edu.cn*

† Electronic supplementary information (ESI) available: Details of SEM images. See DOI: 10.1039/c9ra08975f

In this paper, we constructed a core–shell–shell structure to solve the above-mentioned problems. In this structure, silica has been used as the core and shell material due to its well-known characteristics of easy dispersion and high stability.[31] Firstly, small-sized ceria particles were uniformly deposited on the surface of monodispersed silica nano-spheres. Then, a layer of SiO_2/MPS (3-methacryloxypropyltrimethoxysilane) shell was introduced to isolate the ceria from the external environment, which provides the active site for the subsequent mini-emulsion reaction. The resulting nanoparticles were used to prepare a polyacrylate/M-CeO_2@SiO_2 latex *via* a mini-emulsion polymerization process for outdoor functional coatings. In addition to the original advantages of the fluorine-containing acrylic resin, the latex coating exhibits excellent UV absorption capabilities. Furthermore, due to the increase in surface roughness and the enrichment of the fluorine component on the surface, the hydrophobicity of the coating is also improved.

2. Experimental

2.1 Materials

Cerium nitrate hexahydrate ($Ce(NO_3)_3 \cdot 6H_2O$, ≥99.95%) and commercial ceria (CeO_2, 99.5%) were obtained from Aladdin Industrial Corporation. Tetraethoxysilane (TEOS, AP), hexamethylenetetramine (HMT, ≥99%), *N*-hexadecane (HD, ≥98%), sodium dodecyl sulfate (SDS, CP), and acrylic acid (AA) were bought from Xilong Chemical Co., Ltd (Guangzhou, China). Sodium bicarbonate (≥99.5%), ammonia (25 wt%), hydrogen peroxide (≥30%), and absolute ethanol were obtained from Beijing Chemical Works. 3-Methacryloxypropyltrimethoxysilane (MPS) and dodecafluoroheptyl methacrylate (DFMA) were purchased from Nanjing Xiangqian Chemical Co., Ltd and Harbin Xeogia Fluorine-Silicon Chemical Co., Ltd, respectively. All the above reagents were used as received.

Methyl methacrylate (MMA) and butyl acrylate (BA) were used as monomers which were purified using a neutral alumina column to eliminate inhibitors before use. Ammonium persulfate (APS) was obtained from Tianjin Bodi Chemical Co., Ltd, and was recrystallized before use. SiO_2 with a mean diameter of 310 nm was synthesized in our lab using the Störber method.[32] Deionized water and absolute ethanol were used in all processes.

2.2 Characterization techniques

The morphologies and sizes of all the prepared particles (SiO_2, CeO_2@SiO_2, and M-CeO_2@SiO_2) were characterized using field emission scanning electron microscopy (FESEM, JSM-7500F, Japan) and transmission electron microscopy (TEM, JEM-2100F, JEOL, Japan). The TEM samples were prepared by dispersing the particles into ethanol followed by dropping the suspension onto a carbon-coated Cu grid. Particle sizes were measured directly, taking about 50 particles in the SEM pictures into account using software named Nano measurer. An X-ray diffractometer (XRD, D/MAX-2500RB, Japan) was used to identify the crystal structure using Cu Kα radiation with a scan speed of 6° min^{-1} in the 2θ range from 10° to 100°. Fourier transformed infrared (FT-IR) absorption spectra were recorded on a NEXUS-470 FTIR analyzer (Nicolet, USA) from 4000 cm^{-1} to 500 cm^{-1} at a resolution of 8 cm^{-1}. A UV-3600 ultraviolet transmittance analyzer (Shimadzu, Japan) was used to record the UV-vis absorption spectra of the latex films in the wavelength range of 250–700 nm. The static contact angle of water was measured on the surface of films using a DSA 20 (KRÜSS, Germany) at room temperature. Inorganic nanoparticle films were prepared using the compression method with a powder compressing machine (769YP-15A, Tianjin Keqi High & New Technology Corporation), which pressed nano-powder into round flakes under high pressure. Atom force microscopy (AFM) was used to investigate the surface topography of the latex films. 4 μl water droplets were used and five measurements were done for each example. The films were prepared by dropping 1 ml of emulsion onto each slide and then drying at 60 °C for 3 h. All optical photographs were obtained using a digital camera (Olympus E-PL1, Japan).

2.3 Synthesis of CeO_2@SiO_2 nanoparticles

The deposition of CeO_2 onto SiO_2 is affected by electrostatic attraction in a weak alkaline environment. In a typical experiment, 1 g of the prepared SiO_2 and various amounts of $Ce(NO_3)_3 \cdot 6H_2O$ were added into 60 ml of ethanol in a three-necked flask followed by sonicating for 30 min to make it dispersed. Afterward, 3.23 g HMT and 20 g H_2O were added into the flask with agitation. The solution was stirred for 2 h at a temperature of 75 °C, and then 400 μl H_2O_2 was added to oxidize Ce_2O_3 to CeO_2. The precipitates were centrifuged and washed with absolute ethanol three times before drying at 60 °C overnight in an oven.

2.4 Synthesis of M-CeO_2@SiO_2 nanoparticles

Subsequently, the CeO_2@SiO_2 particles were covered with a mixture of MPS and TEOS, so as to separate CeO_2 from the atmosphere, to prevent the catalytic decomposition of CeO_2. Specifically, 0.2 g CeO_2@SiO_2 was dispersed in a solution of 1.2 g water and 16 g ethanol under constant ultra-sonication for 30 min. After that, 0.3 g TEOS and 0.72 g ammonia were added in sequence. After 5 min, 0.2 g MPS (this amount is based on our previous work[33]) dissolved in 10 ml ethanol was added into the flask. The reaction was carried out at room temperature and aged for 8 h. The resulting M-CeO_2@SiO_2 nanoparticles were centrifuged and then washed three times with ethanol, after which the M-CeO_2@SiO_2 nanoparticles were obtained by drying overnight in an oven at 60 °C.

2.5 Preparation of PFA/M-CeO_2@SiO_2 latex and film

The PFA/M-CeO_2@SiO_2 latex was prepared using a typical mini-emulsion polymerization procedure. As shown in Table 1, the oil phase was prepared by mixing all the monomers, the co-stabilizer (HD) and a certain amount of M-CeO_2@SiO_2 (the amount of M-CeO_2@SiO_2 varied from 0 g to 0.12 g, and the latex was denoted as FPA-0 to FPA-12 accordingly). The mixture was sonicated and stirred by a mechanical agitator for 30 min to disperse the nanoparticles evenly. Then the water phase was

Table 1 Recipes used in the mini-emulsion polymerization

	Component	Weight/g
Oil phase	MMA	4.5
	BA	4.5
	MAA	0.2
	DFMA	0.8
	M-CeO_2@SiO_2	0–0.12[a]
	HD	0.4
Water phase	SDS	0.08
	$NaHCO_3$	0.02
	Deionized water	40

[a] According to the EDS results which are shown in Table S1 (see ESI), 1 g of M-CeO_2@SiO_2 contains approximately 0.395 g of CeO_2.

added into the oil phase and sonicated in an ice bath for 30 min. Afterward, a high-speed shearing machine was used at a speed of 8000 rpm for 30 min to generate a homogeneous mini-emulsion. Finally, the resultant mini-emulsion was transferred into a 100 ml three-necked flask equipped with a thermometer, a reflux condenser, a mechanical agitator and a nitrogen inlet. 10 ml of 1 wt% APS aqueous solution was used as an initiator and the reaction was kept at 75 °C for 6 h.

Latex was spin-coated onto the slides and dried at 60 °C for 3 h to form a film for follow-up tests.

3. Results and discussion

3.1 Preparation of M-CeO_2@SiO_2 nanoparticles

In order to avoid the agglomeration of cerium oxide, improve its dispersion within the coatings, and allow it play the role in the UV absorption, a three layer structure was designed. In the structure, monodispersed SiO_2 particles were used as cores to ensure the even distribution of cerium oxide, and MPS/SiO_2 was used as the shell material to improve the compatibility with the polymer system and prevent the catalytic performance. The particle synthesis diagram is illustrated schematically in Fig. 1a.

SEM/TEM photos in Fig. 1b–f show an intuitive view of the three-layer structure. In Fig. 1b and e, uniform and monodispersed SiO_2 with a diameter of *ca.* 300–320 nm can be clearly observed. When CeO_2 was deposited (Fig. 1c and f), particle sizes increased to 335–350 nm, and a distinctive layer of CeO_2 (the dark layer) can be clearly observed. As for M-CeO_2@SiO_2 (Fig. 1d and g), the particle sizes are further increased to 355–365 nm, with an MPS/SiO_2 layer (the semi-transparent layer) completely covering the surface of CeO_2 to separate CeO_2 from the environment. As is well known, silica particles prepared by the Stöber method usually have smooth surfaces because of the relatively complete hydrolysis and condensation of TEOS in water/ethanol solution.[34] They are negatively charged in neutral or alkaline dispersion. When $Ce(NO_3)_3 \cdot 6H_2O$ is added into SiO_2 dispersion, the positively charged Ce^{3+} ions are attracted to the vicinity of SiO_2 through electrostatic interaction and become deposited on the SiO_2 surface in a weakly alkaline environment. Then the deposited Ce_2O_3 is oxidized to CeO_2 by the addition of H_2O_2. For the purpose of optimizing the cerium loading, the $Ce(NO_3)_3 \cdot 6H_2O$ to SiO_2 mass ratio was varied as follows:

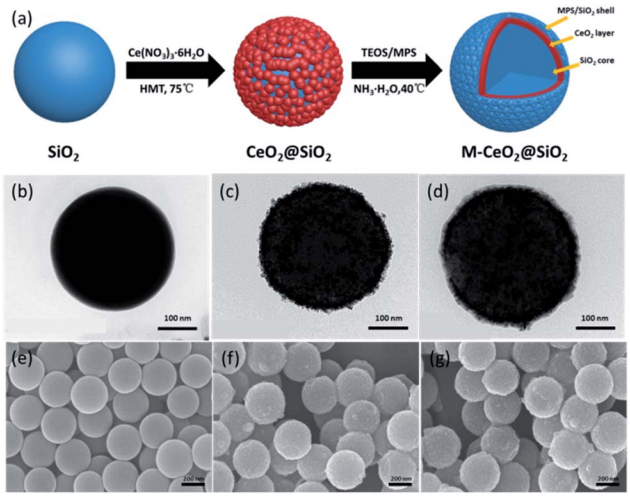

Fig. 1 (a) A schematic drawing of the preparation process of M-CeO_2@SiO_2. FESEM and TEM images of the synthesized nanoparticles: (b) SiO_2-TEM, (c) CeO_2@SiO_2-TEM, (d) M-CeO_2@SiO_2-TEM, (e) SiO_2-SEM, (f) CeO_2@SiO_2-SEM and (g) M-CeO_2@SiO_2-SEM.

$m(Ce(NO_3)_3 \cdot 6H_2O) : m(SiO_2) = 1.5 : 1$, $2 : 1$, $2.5 : 1$, $3 : 1$ and $4 : 1$. As shown in Fig. S1,† when $m(Ce(NO_3)_3 \cdot 6H_2O) : m(SiO_2)$ was below 2, CeO_2 was evenly distributed on the surface of SiO_2. As the amount of Ce^{3+} ions increased, they began to agglomerate. Individual cerium oxide crystals with irregular sizes and shapes are visible. When $m(Ce(NO_3)_3 \cdot 6H_2O) : m(SiO_2) = 2.5 : 1$, larger cerium oxide grains can be clearly observed and randomly distributed over the surface of SiO_2. When the ratio further increased to 3 : 1 or 4 : 1, the ceria grains agglomerated, resulting in the sedimentation of the nanoparticles. Therefore, the ratio of $m(Ce(NO_3)_3 \cdot 6H_2O) : m(SiO_2) = 2 : 1$ was chosen as the preferred ratio.

XRD patterns are typically used to study the phase structure of various nanoparticles. As shown in Fig. 2a, a broad diffraction peak at 23° can be seen in the XRD curve of pure SiO_2, which corresponds to the typical characteristics of amorphous silica. After coating with ceria, four distinct diffraction peaks (28.4°, 32.9°, 47.4°, and 56.2°) can be observed, which correspond to the reflections of the (1 1 1), (2 0 0), (2 2 0) and (3 1 1) planes of the CeO_2 crystal, respectively. This result proves the existence of CeO_2 in CeO_2@SiO_2 and confirms it to have the cubic fluorite structure. The strong and sharp peaks reveal that CeO_2 possesses an intact crystal structure. No new diffraction

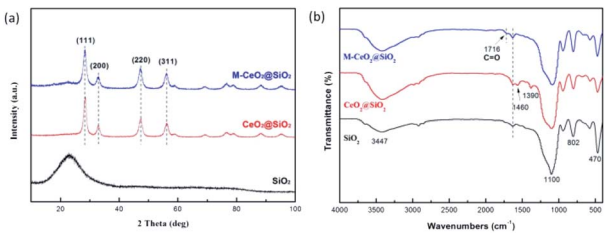

Fig. 2 (a) XRD and (b) FT-IR spectra of pure SiO_2, CeO_2@SiO_2, and M-CeO_2@SiO_2.

peaks appear in M-CeO_2@SiO_2, but the relative intensities of the CeO_2 diffraction peaks decrease, owing to the coverage of MPS/SiO_2. Fig. 2b shows the FT-IR curves of pure SiO_2, CeO_2@SiO_2 and M-CeO_2@SiO_2. The absorption at 1100 cm^{-1} is assigned to the stretching vibration of Si–O–Si, while the peaks at 802 and 470 cm^{-1} belong to the bending vibration of Si–O. The broad peak at around 3447 cm^{-1} is ascribed to the stretching vibration of –OH. The peaks at 1460 and 1390 cm^{-1} are attributed to the Ce–O bond. Compared with CeO_2@SiO_2 and SiO_2, the absorption of the carboxyl group (C=O) at 1716 cm^{-1} in the M-CeO_2@SiO_2 curve demonstrates the successful grafting of MPS on the surface of the CeO_2@SiO_2 nanoparticles.

In summary, the monodispersed three-layer structure nanoparticles were synthesized as anticipated. Silica is the central core, cerium dioxide forms the middle layer and MPS/SiO_2 is the outmost layer.

3.2 Performance of M-CeO_2@SiO_2 nanoparticles

The MPS/SiO_2 shell shielded the catalytic properties of CeO_2, and photo-degradation experiments were carried out to prove it. The results are shown in Fig. 3a. It can be clearly observed that the Rh B concentration decreased rapidly when CeO_2 is not coated. After 4 h of irradiation with a Xe lamp, about 79.44% and 98.2% of Rh B was degraded by pure CeO_2 and CeO_2@SiO_2, respectively. As a comparison, only 31.94% Rh B was degraded in M-CeO_2@SiO_2 suspension, which is even slightly lower than that of the blank sample (35.65%). Throughout the process, the decomposition curve of the M-CeO_2@SiO_2 suspension was almost parallel with that of the blank sample. The tiny gap between the M-CeO_2@SiO_2 suspension and the blank sample arises from the fact that the opaque M-CeO_2@SiO_2 suspension blocked part of the light. It is obvious that nanoparticles with the MPS/SiO_2 layer show no catalytic properties. As a result, the synthesized M-CeO_2@SiO_2 can be safely added into the organic system, avoiding the potential decomposition of the polymer matrix.

The MPS/SiO_2 layer also improves the compatibility of nanoparticles with the polymer latex. It is well known that the compatibility of nanoparticles with the monomer mixture is of vital importance for the stability and global properties of the final emulsion. 1 wt% of pure CeO_2, CeO_2@SiO_2 and M-CeO_2@SiO_2 nanoparticles were dispersed separately into the monomer mixture which was composed of MMA/BA = 50/50 wt%. As shown in Fig. 3b, after a 12 h sedimentation test at room temperature, CeO_2 and CeO_2@SiO_2 nanoparticles precipitated at the bottom of the monomer mixture; however, the M-CeO_2@SiO_2 nanoparticles did not form sediment and exhibited a uniform opaque feature, presenting constant stability and compatibility. The contact angle of the nanoparticles reflected this phenomenon to some extent. As is well known, acrylic monomers are oleophilic monomers, which are incompatible with water. To be dispersed uniformly within acrylic monomers, nanoparticles should also be hydrophobic, too. That means the water contact angle (WCA) should be larger than 90°. Fig. 3c presents the WCAs of the nanoparticles. Obviously, pure CeO_2 and CeO_2@SiO_2 nanoparticles are hydrophilic, and the WCAs are 36.9° and 21.9°, respectively. After modification with MPS, however, the WCA dramatically increased to 112°. This may be attributed to the uniform dispersion of M-CeO_2@SiO_2 nanoparticles amongst the acrylate monomers. The M-CeO_2@SiO_2 nanoparticles are more likely to maintain their stability in the polymer system compared with pure CeO_2 and unmodified CeO_2@SiO_2 nanoparticles.

3.3 Preparation of PF/M-CeO_2@SiO_2 latex coatings

The above-synthesized nanoparticles were applied to the acrylate emulsion system *via* a mini-emulsion polymerization process to improve the performance of polyacrylate resin.

The morphology of the latex particles was observed using TEM to investigate the formation mechanism of the composite films. Hybrid latex containing 1.0 wt% M-CeO_2@SiO_2 nanoparticles was dropped onto a copper grid. As can be observed from Fig. 4a, the hybrid particles show a raspberry-like structure with several polymeric particles grafted onto the surface of the nanoparticles. The amount of PF/M-CeO_2@SiO_2 particles is small because of the low content of the M-CeO_2@SiO_2 nanoparticles. This structure is formed because of the good compatibility between nanoparticles and organic monomers.

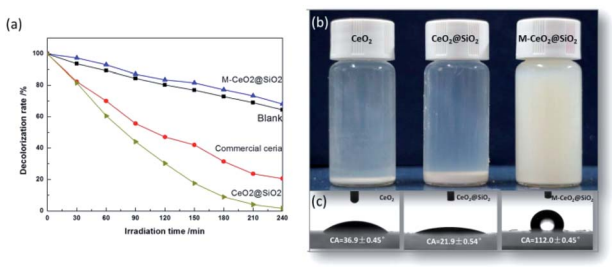

Fig. 3 Performance of the synthesized nanoparticles: (a) the photocatalytic degradation of Rh B; (b) the dispersion of CeO_2, CeO_2@SiO_2 and M-CeO_2@SiO_2 (1 wt%) in monomer mixtures; and (c) the water contact angles of CeO_2, CeO_2@SiO_2 and M-CeO_2@SiO_2.

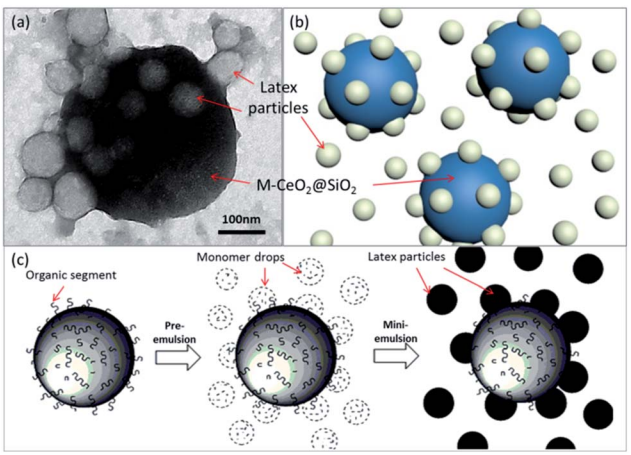

Fig. 4 (a) A TEM image of PF/M-CeO_2@SiO_2 particles; schematic representations of (b) PF/M-CeO_2@SiO_2 particles and (c) the growth of PFA latex particles.

Fig. 4c illustrates the preparation of the PF/M-CeO_2@SiO_2 latex using a mini-emulsion polymerization process. In the pre-emulsification process, the organic segments on the surface of the nanoparticles attract the surrounding acrylic monomers. After that, these monomers polymerize directly to form raspberry-like structures during the mini-emulsion. The uneven distribution of polymeric particles on the M-CeO_2@SiO_2 surface is probably due to steric hindrance among polymeric particles. The raspberry-like structures would benefit the even dispersion of M-CeO_2@SiO_2 particles in the latex system and subsequent coatings (as shown in Fig. S2†).

The chemical composition of the PF/M-CeO_2@SiO_2 film was characterized by FT-IR as shown in Fig. 5. The absorption peaks at 2956 cm^{-1} and 2874 cm^{-1} are the stretching vibrations peaks of C–H, while the peak at 1723 cm^{-1} is assigned to the stretching vibration peak of C=O. Absorption at 3345 cm^{-1} belongs to –OH. Furthermore, the characteristic peaks at 1236 cm^{-1} and 1143 cm^{-1} are the stretching vibration peaks of C–F. Compared with PFA0, few changes can be observed after the incorporation of M-CeO_2@SiO_2 nanoparticles due to the small amount of nanoparticles in the hybrid latex. Only a weak peak at 800 cm^{-1}, which corresponds to Si–O, indicates the existence of M-CeO_2@SiO_2 nanoparticles within fluorinated polyacrylate.

3.4 Performance of PF/M-CeO_2@SiO_2 latex coatings

Due to the excellent UV absorption capacity of ceria, the hybrid films containing M-CeO_2@SiO_2 also show the ability of UV absorption. The UV-vis absorption capacity of hybrid latex films with different M-CeO_2@SiO_2 content was measured, and the results are shown in Fig. 6. Obviously, hybrid latex films containing M-CeO_2@SiO_2 nanoparticles show considerably stronger absorption of light below 600 nm than the pristine film, especially in the wavelength range of 250–400 nm. Furthermore, the UV-vis absorption capacity of the films increases gradually with the amount of nanoparticles present in the final film.

Surface hydrophobicity is an important property of fluoropolymers. Thus, water contact angle measurements were taken to evaluate the wettability properties of PF/M-CeO_2@SiO_2 films, and the results are displayed in Fig. 7. It can be seen that the surface hydrophobicity of the hybrid films significantly improved with a small amount of M-CeO_2@SiO_2 nanoparticles added. As shown in Fig. 7, the bare PFA0 film exhibits an average WCA of 84.2°. When 0.2 wt% M-CeO_2@SiO_2 nanoparticles were added, however, the WCA dramatically increased to 90.5°. When the content of M-CeO_2@SiO_2 was increased further, the hydrophobicity of the hybrid films gradually increased initially, and then decreased. The PFA10 film, which contains about 1.0 wt% M-CeO_2@SiO_2, shows the highest water contact angle of 98.2°. All the hybrid films containing M-CeO_2@SiO_2 show a higher level of surface hydrophobicity than that of PFA0. As is well known, solid surface hydrophobicity is determined by the surface microstructure and chemical composition. The altered WCA data indicate that some changes have taken place on the surface after the addition of M-CeO_2@SiO_2. To investigate the changes, AFM and EDS tests were performed to study the film surface properties.

Fig. 8 shows the AFM height and Rq (root mean square roughness) of the hybrid films. It can be seen that the hybrid films containing M-CeO_2@SiO_2 nanoparticles displayed rougher surfaces than that of PFA0. As shown in Fig. 8a, bare PFA0 shows a rather smooth surface, with Rq = 0.268, and revealed good compatibility of the fluorinated segment with the polyacrylate system. After the addition of M-CeO_2@SiO_2, the

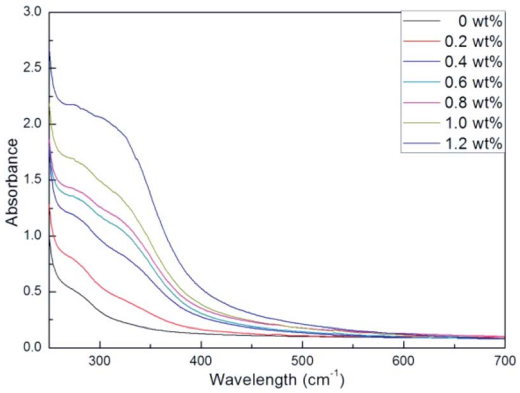

Fig. 6 UV-vis spectra of PF/M-CeO_2@SiO_2 coatings.

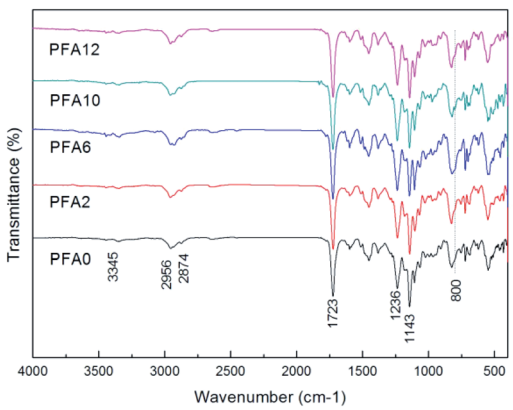

Fig. 5 FT-IR spectra of PF/M-CeO_2@SiO_2 coatings.

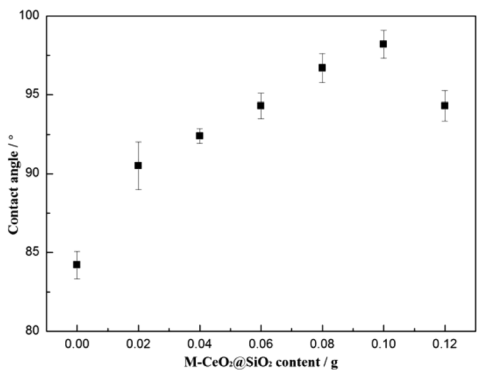

Fig. 7 The water contact angles of PF/M-CeO_2@SiO_2 coatings with various amounts of M-CeO_2@SiO_2 nanoparticles.

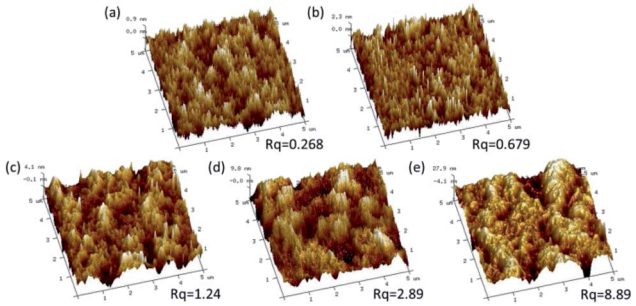

Fig. 8 AFM images of PF/M-CeO_2@SiO_2 coatings: (a) PFA0, Rq = 0.268; (b) PFA2, Rq = 0.679; (c) PFA6, Rq = 1.24; (d) PFA10, Rq = 2.89; and (e) PFA12, Rq = 8.89.

film surface roughness increased. As the M-CeO_2@SiO_2 nanoparticle content increased from 0 wt% to 1 wt%, Rq increased slowly from 0.268 to 2.89. However, as the nanoparticle content continued to increase to 1.2 wt%, there was a dramatic change in the surface roughness, with Rq increasing to 8.89. This sharp increase is likely ascribed to the partial agglomeration of nanoparticles, according to our group's previous work.[35] Although the M-CeO_2@SiO_2 nanoparticles exhibit relatively good compatibility with the polymeric system, when too many nanoparticles are added during the polymerization process, partial agglomeration might happen, resulting in the sharp increase in surface roughness. The Wenzel and Cassie–Baxter models are two well-known classic wetting models that are commonly used to explain the relationship between wettability and surface roughness. According to those theories, the WCA of a hydrophobic surface can be improved by a rough surface, which is consistent with our experimental results.

Table 2 presents the chemical composition at the air-film interface of the PF/M-CeO_2@SiO_2 hybrid films. With the addition of M-CeO_2@SiO_2 into PFA copolymers, a remarkable increase of fluorine content on the film surface can be observed. It can be seen from Table 2 that only 6.80 wt% fluorine content can be detected from the latex film containing no M-CeO_2@SiO_2 nanoparticles. As the M-CeO_2@SiO_2 content increases from 0 wt% to 1.2 wt%, the fluorine content on the film surface increases significantly from 6.80 wt% to 9.45 wt% at first, and then decreases slightly to 8.54 wt%. This result indicates that the addition of M-CeO_2@SiO_2 helps the enrichment of fluorine on the surface because of the unique structure of the hybrid particles. By constructing a raspberry-like structure, parts of the latex particles grow directly on the M-CeO_2@SiO_2 surface. During the film formation process, those latex particles concentrate on the surface along with the M-CeO_2@SiO_2 nanoparticles.[33] Furthermore, the fluorine-containing groups always migrate to the surface during the film formation process due to their relatively low surface energy. By the addition of the nanoparticles, the surface roughness and the specific surface area of the film layer increase, which helps to increase the content of the F element per unit area. A slight decrease of fluorine content when more nanoparticles were added resulted from the partial agglomeration of nanoparticles, as mentioned before.

Table 2 Elemental content of the hybrid film surfaces *via* EDS (wt%)

Sample	PFA0	PFA2	PFA6	PFA10	PFA12
C	63.76	62.57	62.19	63.17	60.58
O	29.28	29.11	27.89	27.89	30.90
F	6.80	7.76	9.45	8.91	8.54

4. Conclusions

Ceria was uniformly incorporated into polymeric matrices and maintained high stability when a three-layer nanoparticle structure was constructed. The synthesized nanoparticles are about 360 nm in diameter. Monodispersed silica spheres with controlled sizes ensure the even distribution of ceria. An MPS/SiO_2 layer protects the catalytic activity of ceria and improves the compatibility between the nanoparticles and the organic matrix. The synthesized M-CeO_2@SiO_2 nanoparticles were incorporated into fluorinated polyacrylate resin *via* a mini-emulsion method. After the addition of M-CeO_2@SiO_2, the hydrophobicity of the hybrid coatings improved significantly from 84.2° to a maximum of 98.2°, due to the enrichment of fluorine and an increase in the surface roughness. Furthermore, the UV absorption capacity of the hybrid coating was improved, as expected, with the use of M-CeO_2@SiO_2. The hybrid coating is a promising candidate material for outdoor coatings.

Conflicts of interest

There are no conflicts to declare.

Acknowledgements

The authors are very grateful for support from the National Natural Science Foundation of China (Grant No. U1637204).

References

1 L. Feng, S. H. Li, Y. S. Li, H. J. Li, L. J. Zhang, J. Zhai, Y. L. Song, B. Q. Liu, L. Jiang and D. B. Zhu, *Adv. Mater.*, 2002, **14**, 1857–1860.
2 J. W. Ha, I. J. Park, S. B. Lee and D. K. Kim, *Macromolecules*, 2002, **35**, 6811–6818.
3 J. Wu, R. Zhang, P. Li, G. Ma, C. Hou and H. Zhang, *J. Coat. Technol. Res.*, 2019, **16**, 681–688.
4 K. Li, X. Zeng, H. Li and X. Lai, *Appl. Surf. Sci.*, 2014, **298**, 214–220.
5 V. Sabatini, E. Pargoletti, V. Comite, M. A. Ortenzi, P. Fermo, D. Gulotta and G. Cappelletti, *Polymers*, 2019, **11**, 1190.
6 S. D. Vacche, S. Forzano, A. Vitale, M. Corrado and R. Bongiovanni, *Int. J. Adhes. Adhes.*, 2019, **92**, 16–22.
7 J. Tsibouklis, P. Graham, P. J. Eaton, J. R. Smith, T. G. Nevell, J. D. Smart and R. J. Ewen, *Macromolecules*, 2000, **33**, 8460–8465.
8 A. Asakawa, M. Unoki, T. Hirono and T. Takayanagi, *J. Fluorine Chem.*, 2000, **104**, 47–51.

9 M. Aguirre, M. Goikoetxea, L. A. Otero, M. Paulis and J. R. Leiza, *Surf. Coat. Technol.*, 2017, **321**, 484–490.
10 H. Xiu, X. Qi, H. Bai, Q. Zhang and Q. Fu, *Polym. Degrad. Stab.*, 2017, **143**, 136–144.
11 A. Ehsani, F. Babaei and M. Nasrollahzadeh, *Appl. Surf. Sci.*, 2013, **283**, 1060–1064.
12 G. Ren, Y. Song, X. Li, B. Wang, Y. Zhou, Y. Wang, B. Ge and X. Zhu, *J. Colloid Interface Sci.*, 2018, **522**, 57–62.
13 M. Aguirre, M. Barrado, M. Iturrondobeitia, A. Okariz, T. Guraya, M. Paulis and J. Ramon Leiza, *Chem. Eng. J.*, 2015, **270**, 300–308.
14 M. Aklalouch, A. Calleja, X. Granados, S. Ricart, V. Boffa, F. Ricci, T. Puig and X. Obradors, *Sol. Energy Mater. Sol. Cells*, 2014, **120**, 175–182.
15 C. Sun, H. Li and L. Chen, *Energy Environ. Sci.*, 2012, **5**, 8475–8505.
16 T. Masui, M. Yamamoto, T. Sakata, H. Mori and G. Adachi, *J. Mater. Chem.*, 2000, **10**, 353–357.
17 S. Xie, Z. Wang, F. Cheng, P. Zhang, W. Mai and Y. Tong, *Nano Energy*, 2017, **34**, 313–337.
18 S. Parwaiz, M. M. Khan and D. Pradhan, *Mater. Express*, 2019, **9**, 185–202.
19 M. Aguirre, E. J. Salazar-Sandoval, M. Johansson, A. Ahniyaz, M. Paulis and J. Ramon Leiza, *J. Mater. Chem. A*, 2014, **2**, 20280–20287.
20 H. Ye, L. Zhu, W. Li, G. Jiang, H. Liu and H. Chen, *Chem. Eng. J.*, 2017, **321**, 268–276.
21 M. Aguirre, M. Paulis, J. Ramon Leiza, T. Guraya, M. Iturrondobeitia, A. Okariz and J. Ibarretxe, *Macromol. Chem. Phys.*, 2013, **214**, 2157–2164.
22 R. Francis, N. Joy, E. P. Aparna and R. Vijayan, *Polym. Rev.*, 2014, **54**, 268–347.
23 L. Qi, A. Sehgal, J. C. Castaing, J. Fresnais, J. F. Berret and J. P. Chapel, *Redispersible Hybrid Nanopowders: Cerium Oxide Nanoparticle Complexes with Phosphonated-PEG Oligomers*, 2008.
24 O. Parlak and M. M. Demir, *ACS Appl. Mater. Interfaces*, 2011, **3**, 4306–4314.
25 B. Chanteau, J. Fresnais and J. F. Berret, *Langmuir*, 2009, **25**, 9064–9070.
26 I. A. Siddiquey, T. Furusawa, Y.-i. Hoshi, E. Ukaji, F. Kurayama, M. Sato and N. Suzuki, *Appl. Surf. Sci.*, 2008, **255**, 2419–2424.
27 S. C. Zhang and X. G. Li, *Powder Technol.*, 2004, **141**, 75–79.
28 A. Guerrero-Martinez, J. Perez-Juste and L. M. Liz-Marzan, *Adv. Mater.*, 2010, **22**, 1182–1195.
29 F. Dang, N. Enomoto, J. Hojo and K. Enpuku, *Ultrason. Sonochem.*, 2010, **17**, 193–199.
30 G. Marcelo, E. Perez, T. Corrales and C. Peinado, *J. Phys. Chem. C*, 2011, **115**, 25247–25256.
31 J. Wang, Z. H. Shah, S. Zhang and R. Lu, *Nanoscale*, 2014, **6**, 4418–4437.
32 L. Tian, W. Li, H. Ye, L. Zhu, H. Chen and H. Liu, *Surf. Coat. Technol.*, 2019, **377**, 892–899.
33 W. Yang, L. Zhu and Y. Chen, *RSC Adv.*, 2015, **5**, 58973–58979.
34 W. Stober, A. Fink and E. Bohn, *J. Colloid Interface Sci.*, 1968, **26**, 62–69.
35 W. Yang, L. Zhu, Y. Chen, H. Ye and Z. Ye, *Colloids Surf., A*, 2015, **484**, 62–69.

